Simple algorithms for solving steady-state frictional rolling contact problems in two and three dimensions

Gérard-Philippe Zéhil[a,*], Henri P. Gavin[a]

[a] *Department of Civil and Environmental Engineering, Duke University, 121 Hudson Hall, Box 90287, Research Drive, Durham, NC 27708-0287, United States*

Abstract

This paper presents simple, yet robust and efficient algorithms for solving steady-state, frictional, rolling/sliding contact problems, in two and three dimensions. These are alternatives to powerful, well established, but in particular instances, possibly 'cumbersome' general-purpose numerical techniques, such as finite-element approaches based on constrained optimization. The cores of the solvers rely on very general principles: (i) resolving motional conflicts, and (ii) eliminating unacceptable surface tractions. The proposed algorithms are formulated in the context of small deformations and applied to the cases of a rigid cylinder and a rigid sphere rolling on a linear viscoelastic layer of finite thickness, in two and three dimensions, respectively. The underlying principles are elucidated, relevant mathematical expressions derived and details given about corresponding implementation techniques. The proposed contact algorithms can be extended to more general settings involving a deformable indenter, material nonlinearities and large deformations.

Keywords: Rolling contact, cylinder, sphere, viscoelastic layer, Coulomb's friction, stick/slip contact, numerical algorithm.

---

1. Introduction

Contact problems involve surface to surface mechanical interactions between one or more physical bodies, which in general, are deformable. The contact surface as well as the corresponding boundary conditions are usually unknown and left to be determined as part of the solution. Mechanical behaviors of touching objects are defined by their various shapes, bulk material properties, surface characteristics and by external actions. These primary factors may in turn depend upon other physical parameters, such as temperature and time, but also upon the state of contact. Reciprocally, the mechanical response of each individual object has an influence on the dimensions of the contact surfaces as well as on the intensity and nature of surface interactions. Contact problems are hence characterized by intricate and highly nonlinear dependences. They are consequently regarded as being among the most difficult to model and solve (e.g. Zienkiewicz and Taylor, 2005).

Full analytical solutions to contact problems exist in some standard settings (e.g. Galin and Gladwell, 2008). Very useful asymptotic expansions have also been derived in limiting cases (e.g. Jaffar, 1997, 2008). However, more often than not, contact problems require numerical modeling and solution. Well established finite element methods are frequently used to this end while specific types of constraints arising from contact are commonly enforced using optimization techniques based on Lagrange multipliers and penalty methods. A dense review of some of the most successful finite element solving strategies can be found, for instance, in Zienkiewicz and Taylor (2005). Nevertheless, despite their power and broad scope of application, the fact remains that in many particular instances, the practical implementation of such methods can be unnecessarily complicated.

Simpler and more convenient alternatives exist, such as the approach proposed by Kalker (1979), which is based on the Hertz elastic theory of contact (Hertz, 1881). The high computational efficiency of such approaches results

---

[*] Corresponding author

Email address: `gerard.zehil@duke.edu` (Gérard-Philippe Zéhil) from the use of existing analytical solutions based on simplifying assumptions and therefore limiting their scope of application. In its original form, Kalker's approach assumes that the contact surface is elliptic and that the distribution of normal stresses is of the Hertz's form. Its current implementation in the "CONTACT" program (Vollebregt, 2012) relaxes these assumptions but still approximates the contacting bodies by linear elastic half-spaces to decouple the contact problem from the global simulation. In this context, surface displacements are estimated according to the analytical solution of Boussinesq and Cerruti (Love, 1927) for an elastic half-space. Kalker's contact theory relies on the principle of superposition and the reciprocity theorem. It is therefore limited to linear elasticity and secondarily, to linear viscoelasticity. The latter is applied only to the contact surface but not to the bulk of the contacting bodies. Instead, the responses of the bodies are approximated using the elastic half-space approach. In brief, the Kalker theory is based on the assumptions that the contacting bodies are linear elastic and that the contact surface is flat and small with respect to their typical dimensions. Many practical settings do not satisfy these assumptions, for instance, in the case of problems involving thin viscoelastic layers.

The present work focuses on presenting simple, yet robust and efficient algorithms for solving steady-state, frictional, rolling (or sliding) contact problems, in two and three dimensions. The cores of the solvers rely on very general principles: (i) resolving normal and tangential motional conflicts between the contacting bodies, and (ii) eliminating unacceptable normal and tangential surface tractions. The proposed algorithms are formulated in the context of small deformations and applied to the cases of a rigid cylinder and a rigid sphere rolling on a linear viscoelastic layer of finite thickness, in two and three dimensions, respectively. The formulations presented can be easily extended to handle stationary or steady-state rolling/sliding contact problems involving a deformable indenter or to more general settings, such as problems involving materials nonlinearities and large deformations.

2. Problem setting and conventions

Figure 1 shows a round and undeformable object, which may be a cylinder or a sphere. This object is moving to the right in steady state, at a linear speed V_s along direction x, while in contact with a deformable layer on which it may be rolling (at a rotational speed Ω) or sliding, in the presence of surface friction.

Frame $O'x'y'z'$ corresponds to a material coordinate system that is attached to the subbase. However, the (steady-state) contact problem is considered in a moving frame of reference $Oxyz$, traveling along with the object, and in which material time derivatives are expressed such that time becomes an implicit variable

$$\frac{D}{Dt} = -V_s \frac{\partial}{\partial x} \; ; \; \frac{D^2}{Dt^2} = V_s^2 \frac{\partial^2}{\partial x^2}. \tag{1}$$

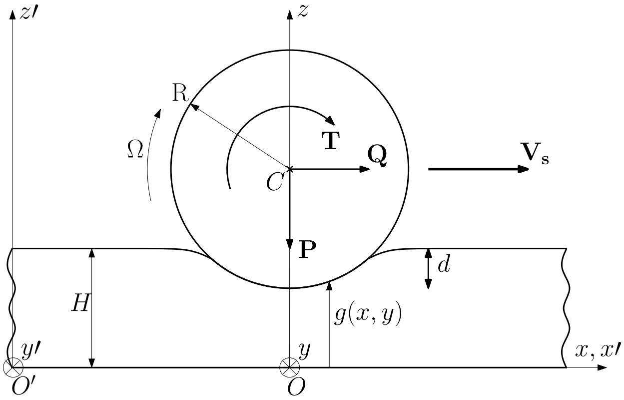

Figure 1: General model and coordinate systems

For definiteness and without prejudice to the generality of the foregoing material, we will consider a linear viscoelastic and incompressible foundation of finite thickness H, bounded to a rigid substrate. In a two dimensional setting (the case of a cylinder), plane-strain conditions are applied. It is furthermore assumed that surface friction follows Coulomb's law, with a constant friction coefficient μ. In the context of linear viscoelasticity, the layer must incur relatively small deformations. Consequently, wherever deemed convenient, relevant physical quantities (e.g. the stress tensor $\boldsymbol{\sigma}$ and the small-strain tensor $\boldsymbol{\epsilon}$) may be expressed in the reference frame or in the current frame, indifferently.

In our general case, the moving object will be subjected to the following external action components, acting in the vertical plane of movement and expressed at its axis C: (i) a driving horizontal force Q acting positively from left to right, (ii) a vertical load P, positive downwards, and (iii) a driving torque T, positive clockwise. The moving object is also subjected to the unknown reaction of the subbase, consisting of vertical and horizontal surface traction fields: $\sigma_z(x, y, H)$, $\tau_{xz}(x, y, H)$ and $\tau_{yz}(x, y, H)$. As demonstrated for instance by Munisamy et al. (1991), shear tractions influence the contact pressure distribution and vice-versa. The main goal behind solving the rolling contact problem is to determine those fully coupled surface tractions, along with the corresponding foundation surface displacement fields (i.e. $u(x, y, H)$, $v(x, y, H)$ and $w(x, y, H)$), as well as the rotational speed Ω and the indentation d. In the absence of friction, the 'frictional' implementations given in this manuscript are readily adapted and reduced by eliminating unnecessary equations and solving for the normal contact-stress distribution only, using vertical equilibrium, which excludes the rotational quantities T and Ω that are indeterminate.

In the three dimensional case, the candidate contact surface is discretized as shown in figure 2 with a total number of $N_T = K_x K_y$ nodes. Similar conventions apply in two dimensions. The basic ideas developed in this work may be applied to diverse settings and implemented in various numerical contexts, for instance, as part of a finite element or a finite difference model. The contact solving algorithms are presented and discussed in the subsequent sections, assuming that the layer is modeled by means of a boundary element formulation of the form

$$\mathbf{CF} = \mathbf{D}, \tag{2}$$

where $\mathbf{C}$ is a compliance matrix characterizing the mechanical behavior of the discretized candidate contact surface on the layer's upper boundary, $\mathbf{F}$ is a nodal surface force vector and $\mathbf{D}$ is the corresponding nodal surface displacement vector. Suitable methods for building matrix $\mathbf{C}$ are given for instance by Qiu (2006) and Zéhil and Gavin (2013b), in two and three dimensions respectively. Other approaches may be used as well. In the three dimensional case, $\mathbf{F}$ and $\mathbf{D}$ are partitioned into subvectors as follows

$$\mathbf{F} = \left\langle \mathbf{F}_W^T, \mathbf{F}_U^T, \mathbf{F}_V^T \right\rangle^T = \text{ vector of nodal forces}, \tag{3}$$

$$\mathbf{D} = \left\langle \mathbf{W}^T, \mathbf{U}^T, \mathbf{V}^T \right\rangle^T = \text{ vector of nodal displacements}, \tag{4}$$

each subvector containing nodal components in a given direction. The full compliance matrix $\mathbf{C}$ is of dimensions $(3N_T \times 3N_T)$. Following the Cartesian spatial directions and in accordance with the previous ordering of the nodal subvectors in (3) and (4), matrix $\mathbf{C}$ may be partitioned into nine $(N_T \times N_T)$ submatrices $\mathbf{C}_{PQ}$ where indices $P, Q \in \{U, V, W\}$. Equation (2) may hence be written in the form

$$\begin{bmatrix} \mathbf{C}_{WW} & \mathbf{C}_{WU} & \mathbf{C}_{WV} \\ \mathbf{C}_{UW} & \mathbf{C}_{UU} & \mathbf{C}_{UV} \\ \mathbf{C}_{VW} & \mathbf{C}_{VU} & \mathbf{C}_{VV} \end{bmatrix} \begin{bmatrix} \mathbf{F}_W \\ \mathbf{F}_U \\ \mathbf{F}_V \end{bmatrix} = \begin{bmatrix} \mathbf{W} \\ \mathbf{U} \\ \mathbf{V} \end{bmatrix}. \tag{5}$$

As illustrated on figure 2, the nodal force vector components ${F_W}^N$, ${F_U}^N$ and ${F_V}^N$, for $N = 1 \ldots N_T$, in the moving Cartesian frame of reference, may be expressed in terms of their spherical counterparts ${F_R}^N$, ${F_\Phi}^N$ and ${F_\Theta}^N$ using the following coordinate transformation

$$\begin{bmatrix} {F_W}^N \\ {F_U}^N \\ {F_V}^N \end{bmatrix} = \begin{bmatrix} \cos(\phi) & \sin(\phi) & 0 \\ -\cos(\theta)\sin(\phi) & \cos(\theta)\cos(\phi) & -\sin(\theta) \\ -\sin(\theta)\sin(\phi) & \sin(\theta)\cos(\phi) & \cos(\theta) \end{bmatrix} \begin{bmatrix} {F_R}^N \\ {F_\Phi}^N \\ {F_\Theta}^N \end{bmatrix}. \tag{6}$$

The normal and tangential stress fields corresponding to the spherical nodal force vectors $\mathbf{F}_R$, $\mathbf{F}_\Phi$ and $\mathbf{F}_\Theta$ are designated by $\sigma_r(x, y, H)$, $\tau_{\phi r}(x, y, H)$ and $\tau_{\theta r}(x, y, H)$, respectively.

As a consequence of the small-strain assumption resulting from linear viscoelasticity, one may identify *normal* with *vertical* components and *tangent* with *horizontal* components of surface fields. Equivalently, setting $\phi \approx 0$,

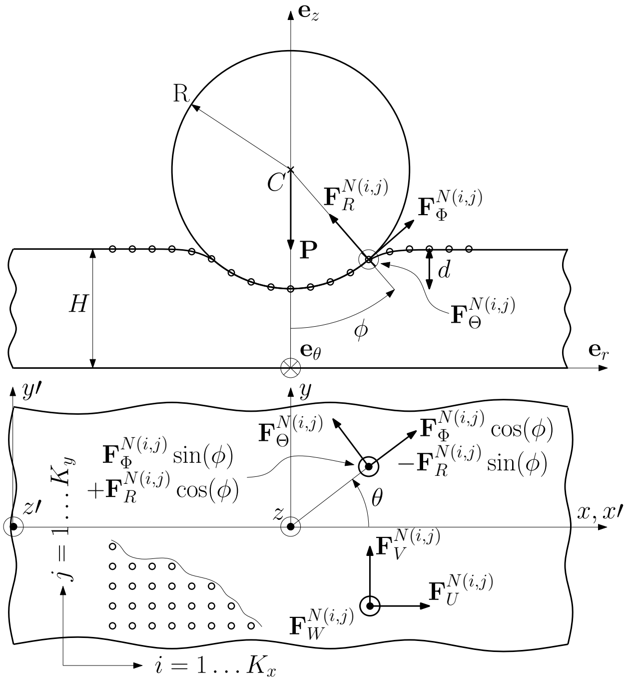

Figure 2: Discretization and nodal forces in two coordinate systems [a]

---

[a] a_x and a_y denote the nodal spacing in directions x and y, respectively.

system (6) would reduce to

$$\begin{bmatrix} {F_W}^N \\ {F_U}^N \\ {F_V}^N \end{bmatrix} \approx \begin{bmatrix} 1 & 0 & 0 \\ 0 & \cos(\theta) & -\sin(\theta) \\ 0 & \sin(\theta) & \cos(\theta) \end{bmatrix} \begin{bmatrix} {F_R}^N \\ {F_\Phi}^N \\ {F_\Theta}^N \end{bmatrix}. \tag{7}$$

Equation (7) is invoked in the following two instances *only*: (i) in the 2D case of section 3, F_R and F_Φ are equated to F_W and F_U in equation (8), and (ii) in the 3D case of section 4, it is assumed that Coulomb's inequality applies to F_W, F_U and F_V instead of F_R, F_Φ and F_Θ in expression (38). Conversely, the approximation $\phi \approx 0$ applies to the displacement fields throughout. The following notational conventions are furthermore adopted:

- adding a scalar to an array results in adding that scalar to each of the array's components,
- each component of an array is individually raised at a given power κ when (κ) is displayed between parenthesis.

3. 2D algorithm for frictional rolling contact

In the 2D problem of a cylinder rolling across a viscoelastic layer, the discretized candidate contact surface is (conceptually) divided into three non-overlapping domains: two free regions denoted by the subscripts 1 and 3, separated by an initially continuous contact area designated by the subscript 2. The nodal position vector $\mathbf{x}$ is hence partitioned into three subvectors, i.e. $\mathbf{x} = \left\langle \mathbf{x}_1^T, \mathbf{x}_2^T, \mathbf{x}_3^T \right\rangle^T$. This is also reflected in the boundary element constitutive equation, written as

$$\begin{bmatrix} \mathbf{C}_{WW,11} & \mathbf{C}_{WW,12} & \mathbf{C}_{WW,13} & \mathbf{C}_{WU,11} & \mathbf{C}_{WU,12} & \mathbf{C}_{WU,13} \\ \mathbf{C}_{WW,21} & \mathbf{C}_{WW,22} & \mathbf{C}_{WW,23} & \mathbf{C}_{WU,21} & \mathbf{C}_{WU,22} & \mathbf{C}_{WU,23} \\ \mathbf{C}_{WW,31} & \mathbf{C}_{WW,32} & \mathbf{C}_{WW,33} & \mathbf{C}_{WU,31} & \mathbf{C}_{WU,32} & \mathbf{C}_{WU,33} \\ \mathbf{C}_{UW,11} & \mathbf{C}_{UW,12} & \mathbf{C}_{UW,13} & \mathbf{C}_{UU,11} & \mathbf{C}_{UU,12} & \mathbf{C}_{UU,13} \\ \mathbf{C}_{UW,21} & \mathbf{C}_{UW,22} & \mathbf{C}_{UW,23} & \mathbf{C}_{UU,21} & \mathbf{C}_{UU,22} & \mathbf{C}_{UU,23} \\ \mathbf{C}_{UW,31} & \mathbf{C}_{UW,32} & \mathbf{C}_{UW,33} & \mathbf{C}_{UU,31} & \mathbf{C}_{UU,32} & \mathbf{C}_{UU,33} \end{bmatrix} \begin{bmatrix} \mathbf{F}_{W,1} \\ \mathbf{F}_{W,2} \\ \mathbf{F}_{W,3} \\ \mathbf{F}_{U,1} \\ \mathbf{F}_{U,2} \\ \mathbf{F}_{U,3} \end{bmatrix} = \begin{bmatrix} \mathbf{W}_1 \\ \mathbf{W}_2 \\ \mathbf{W}_3 \\ \mathbf{U}_1 \\ \mathbf{U}_2 \\ \mathbf{U}_3 \end{bmatrix}, \tag{8}$$

where $\mathbf{F}_{W,1}$, $\mathbf{F}_{W,3}$, $\mathbf{F}_{U,1}$ and $\mathbf{F}_{U,3}$ are null vectors. In this two-dimensional case, it is assumed that the constitutive equations of the layer apply in the current configuration, which is a valid assumption under small deformations. Consequently, $\mathbf{F}_R$ and $\mathbf{F}_\Phi$ may be equated to $\mathbf{F}_W$ and $\mathbf{F}_U$ in equation (8). One advantage of such a formulation is that it yields directly-exploitable normal and tangential nodal force fields.

3.1. 2D normal-contact subroutine

For a two-dimensional model in the plane “Oxz”, the normal contact boundary conditions may be expressed as

$$H + w(x, H) < g(x) \text{ if } \sigma_r = 0, \tag{9}$$

$$H + w(x, H) = g(x) \text{ if } \sigma_r < 0, \tag{10}$$

where $g(x)$ corresponds to an analytical expression for the lower surface of the moving rigid body. For for a cylinder of radius R and center C

$$g(x) = z_c - \sqrt{R^2 - x^2}. \tag{11}$$

The normal-contact subroutine is based on equation number 2 in system (8). It operates in two phases, A and B.

Phase A: given a meshed candidate contact surface and a tangent contact-stress distribution (i.e. $\mathbf{F}_\Phi$ is known), the algorithm initially attempts applying the vertical load P on the smallest allowable area, as determined by the discretization, since rolling objects and the layer have non-conforming surfaces. If, at any given iteration, the current contact area is too small, the foundation material will significantly swell on the sides, thus interfering geometrically with the shape of the moving object. Hence, the currently-free nodes are probed individually for geometrical conflicts using (9) and each interfering node is added to the set of contact nodes. Consequently, the contact area grows during phase A while the algorithm is resolving geometrical conflicts.

Phase B: after all geometrical conflicts have been resolved, the current contact area is probed for normal positive tractions. Positive tractions are suppressed by setting free the corresponding nodes, as non-adhesive contact is assumed. Alternatively, an adhesion threshold may be readily set. While iterating in phase B, the contact area mainly shrinks as the algorithm is working on suppressing tensile tractions. If a geometrical conflict arises while in phase B, it is given priority and resolved by shifting back to phase A, and so on.

At each iteration of both phases A and B, the following linear system, augmented with the penetration d, is solved

$$\begin{bmatrix} \mathbf{C}_{WW,22} & \mathbf{1}_n \\ \left(1 - \left(\frac{\mathbf{x}_2}{R}\right)^{(2)}\right)^{(1/2)} & 0 \end{bmatrix} \begin{bmatrix} \mathbf{F}_{R,2} \\ d \end{bmatrix} = \begin{bmatrix} R - \left(R^2 - \mathbf{x}_2^{(2)}\right)^{(1/2)} - \mathbf{C}_{WU,22}\mathbf{F}_{\Phi,2} \\ -P - \frac{\mathbf{x}_2^T \mathbf{F}_{\Phi,2}}{R} \end{bmatrix}, \tag{12}$$

where n is the number of contact nodes at a given iteration and $\mathbf{1}_n$ corresponds to a column vector with n unit components. The first n equations in system (12) reflect the fact that the vertical displacement of the layer across the contact area, i. e. $\mathbf{W}_2$, follows the object’s lower profile given by (11). The last (additional) equation corresponds to the equilibrium of forces in the vertical direction.

In some practical situations, the penetration d is given directly while the vertical load P is unknown. This case is readily solved by removing the last equation from system (12). The global approach remains however unchanged and P is determined by vertical force equilibrium, after the solution has been found.

3.2. 2D stick-slip subroutine

Given our assumptions pertaining to friction, the tangential contact boundary conditions for a two-dimensional model in plane “Oxz” are given by

$$\left|\tau_{\phi r}(x, H)\right| < -\mu\sigma_r(x, H) \text{ if } w_t = 0, \tag{13}$$

$$\tau_{\phi r}(x, H) = -\mu\sigma_r(x, H)\,\mathrm{sgn}(w_t) \text{ otherwise}, \tag{14}$$

involving the coefficient of solid friction μ for the interface, as well as the differential tangential speed across the contact area, i.e.

$$w_t = V_s\left(1 + \frac{\partial u}{\partial x}(x, H)\right) - R\Omega. \tag{15}$$

Inequality (13) is verified across contact regions that are characterized by the absence of relative movement between touching points, while equality (14) is enforced in contact areas that are in relative motion.

The stick-slip subroutine is based on equation number 5 of system (8). Given a fixed contact area and a normal stress field, as determined by the normal-contact subroutine (i.e. $\mathbf{F}_{R,2}$ is known), the stick-slip algorithm first assumes that all the contact nodes are in a state of stick-contact. It then solves iteratively for the distribution of tangent contact-stresses (or $\mathbf{F}_{\Phi,2}$) and the rotational speed Ω. Surface shear forces computed from a given solution iterate are compared with the limiting friction at each node. All stick-contact nodes subjected to a nodal shear force exceeding Coulomb's friction are switched to slip-contact nodes at the next iteration.

In practice, at each iteration, the stick-slip algorithm solves a linear system for the unknown tangent nodal forces at the stick-contact nodes $\mathbf{F}_{\Phi,2}(s)$, given the fact that tangent nodal forces at the slipping nodes $\mathbf{F}_{\Phi,2}(\bar{s})$ are defined by the limiting friction. The corresponding set of equations is further augmented with the rotational speed Ω and a displacement of reference u_{ref}, matching the horizontal displacement of the leading edge stick-contact node. The resulting system is written as follows

$$\begin{bmatrix} -\mathbf{C}_{\mathbf{UU},\mathbf{22}}(s,s) & -\frac{R}{V_s}\mathbf{q_2} & \mathbf{1}_{nst} \\ \mathbf{1}_{nst}^T & 0 & 0 \\ \mathbf{h} & \frac{aR}{V_s} & 1 \end{bmatrix} \begin{bmatrix} \mathbf{F}_{\Phi,2}(s) \\ \Omega \\ u_{ref} \end{bmatrix} = \begin{bmatrix} \mathbf{q}_1 - \mathbf{q}_2 \\ -\frac{T}{R} - \sum(\mathbf{F}_{\Phi,2}(\bar{s})) \\ a + \delta \end{bmatrix}, \tag{16}$$

where

- nst is the number of stick-contact nodes at a given iteration and $\mathbf{1}_{nst}$ corresponds to a column vector with nst unit components,
- the arguments "s" and "$\bar{s}$" stand for extracting from a given array the rows/columns corresponding to stick and slip-contact nodes respectively. Alternatively, the argument " : " stands for "all" lines or columns,
- the subscript "ref" refers to the leading edge stick-contact node: i_{ref} corresponds to its index in the subset of contact nodes, A_{ref} corresponds to its global node number and $x_{ref} = \mathbf{x}_2(i_{ref})$ to its position. As previously mentioned, $u_{ref} = \mathbf{U}_2(i_{ref})$ is the horizontal displacement field at that node,
- $\mathbf{q}_1$, $\mathbf{q}_2$, $\mathbf{h}$ and δ are defined for convenience as follows, depending on whether the leading edge contact node has slipped (case A) or not (case B):
  - $\mathbf{q}_1 = \mathbf{C}_{UW,22}(s,:)\mathbf{F}_{R,2} + \mathbf{C}_{UW,22}(s,\bar{s})\mathbf{F}_{\Phi,2}(\bar{s})$,
  - $\mathbf{q}_2 = x_{ref} - \mathbf{x}(s)$,
  - $\mathbf{h} = \begin{cases} -\mathbf{C}_{UU,22}(i_{ref}+1, s) & \text{in case A,} \\ -\mathbf{C}_{UU,32}(1, s) & \text{in case B,} \end{cases}$
  - $\delta = \begin{cases} \mathbf{C}_{UW,22}(i_{ref}+1,:)\mathbf{F}_{R,2} + \mathbf{C}_{UU,22}(i_{ref}+1,\bar{s})\mathbf{F}_{\Phi,2}(\bar{s}) & \text{in case A,} \\ \mathbf{C}_{UU,32}(1,\bar{s})\mathbf{F}_{\Phi,2}(\bar{s}) + \mathbf{C}_{UW,32}(1,:)\mathbf{F}_{R,2} & \text{in case B.} \end{cases}$

The first nst equations in system (16) reflect the fact that the horizontal elongational strain $\frac{du}{dx} = \frac{\partial u}{\partial x}(x, H)$ remains constant across all stick-contact zones. This is true because the differential tangent speed $w_t = V_s\left(1 + \frac{du}{dx}\right) - R\Omega$ is equal to zero across the sticking interface while V_s and Ω are global constants. The last two equations cover for the the additional unknowns Ω and u_{ref}:

- equation $nst + 1$ reflects the fact that the tangent contact-stress distribution equilibrates the driving torque, or equivalently
$$T = -\sum \mathbf{F}_{\Phi,2} R, \tag{17}$$
- equation $nst + 2$ enforces continuity, as suggested by Qiu (2006), of the horizontal elongational strain on both sides of the leading edge stick-contact node. This is done by means of a finite difference expression
$$\frac{du}{dx}(x_{ref}) = \frac{\mathbf{U}(A_{ref}+1) - u_{ref}}{a}, \tag{18}$$

where a is the spacing between nodes. In many practical applications, the driving torque T is related to the horizontal driving force Q. Commonly, only Q is applied at the top of the rolling object, hence generating a torque $T = QR$. In the latter case, system (16) becomes

$$\begin{bmatrix} -\mathbf{C}_{UU,22}(s,s) & -\frac{R}{V_s}\mathbf{q}_2 & \mathbf{1}_{nst} \\ \mathbf{q}_3(s) & 0 & 0 \\ \mathbf{h} & \frac{aR}{V_s} & 1 \end{bmatrix} \begin{bmatrix} \mathbf{F}_{\Phi,2}(s) \\ \Omega \\ u_{ref} \end{bmatrix} = \begin{bmatrix} \mathbf{q}_1 - \mathbf{q}_2 \\ -\frac{\mathbf{x}_2^T \mathbf{F}_{R,2}}{R} - \mathbf{q}_3^T(\bar{s})\mathbf{F}_{\Phi,2}(\bar{s}) \\ a + \delta \end{bmatrix},$$

where $\mathbf{q}_3$ is defined for convenience as

$$\mathbf{q}_3 = 1 + \left(1 - \left(\frac{\mathbf{x}_2}{R}\right)^{(2)}\right)^{(\frac{1}{2})}. \tag{19}$$

3.3. 2D combined algorithm

The normal-contact subroutine determines the contact surface and the corresponding normal stress distribution given a tangent stress field on the foundation's surface. Alternatively, the stick-slip subroutine determines the slipping regions of a contact area and the corresponding tangent stress distribution given the normal stress field. These two subroutines are therefore combined in a loop that starts by assuming $\mathbf{F}_\Phi = 0$ and converges towards the actual solution of the frictional rolling contact problem.

If needed, the rolling resistance may be computed, after convergence, according to the expression below

$$R_r = -\frac{\mathbf{x}^T \mathbf{F}_R}{R} + \mathbf{F}_\Phi^T \left(1 - \left(\frac{\mathbf{x}}{R}\right)^{(2)}\right)^{(\frac{1}{2})} + \frac{T\Omega}{V_s}. \tag{20}$$

The methodology described in section 3.1 was implemented and tested on a two-dimensional model of a rigid cylinder, rolling in steady-state on an incompressible viscoelastic foundation of finite thickness. It was found to be robust and efficient: full convergence, based on the relative change in all the outputs, was typically obtained in 5 iterations.

4. 3D algorithm for frictional rolling contact

Using a similar approach to the one described in section 3, the discretized candidate contact surface, which is now two-dimensional, is conceptually divided into two separate regions: an initially continuous contact area (referred to by "c") surrounded by an external free surface (referred to by "$\bar{c}$"). At any given iteration of the algorithms that are subsequently described, the arguments c and $\bar{c}$ stand for extracting from a given array the lines/columns corresponding to contact nodes and free nodes, respectively. The constitutive equation used for reference is equation (5).

In the three-dimensional case, working with Cartesian quantities proves to be more convenient since it avoids composing expressions (5) and (7) with varying angles ϕ and θ across the contact surface. Results expressed in Cartesian form are furthermore easier to interpret. If normal and tangential stress fields are specifically needed, the Cartesian results can be transformed into spherical form using equation (6).

4.1. 3D normal-contact subroutine

The method presented in section 3.1 is fairly easily extended and adapted to a three dimensional setting. This is done using notations introduced in section 4 along with similar conventions to the ones that were used throughout section 3. The following linear system, augmented with the penetration d, is solved at each iteration of both phases A and B

$$\begin{bmatrix} \mathbf{C}_{WW}(c,c) & \mathbf{1}_n \\ \mathbf{1}_n^T & 0 \end{bmatrix} \begin{bmatrix} \mathbf{F}_W(c) \\ d \end{bmatrix} = \begin{bmatrix} \mathbf{q}_4(c) - \mathbf{C}_{WU}(c,:)\mathbf{F}_U - \mathbf{C}_{WV}(c,:)\mathbf{F}_V \\ -P \end{bmatrix}, \tag{21}$$

where, for the purposes of the normal-contact subroutine, $\mathbf{F}_U$ and $\mathbf{F}_V$ are considered as given nodal force fields in directions x and y respectively, while the vertical force field $\mathbf{F}_W(c)$ is equal to $\mathbf{0}$. Vector $\mathbf{q}_4$ is defined for convenience as

$$\mathbf{q}_4 = R - \left(R^2 - \mathbf{x}^{(2)} - \mathbf{y}^{(2)}\right)^{(1/2)}. \tag{22}$$

4.2. 3D stick-slip subroutine

Given a contact surface along with the corresponding nodal vertical force field $\mathbf{F}_W$, the three-dimensional stick-slip subroutine determines the regions where slipping occurs and returns the nodal horizontal force fields $\mathbf{F}_U$ and $\mathbf{F}_V$ as well as the the rotational speed Ω.

The two equations below are first extracted from system (5), for stick-contact nodes (s, c), at any given iteration of the stick-slip subroutine

$$\mathbf{C}_{UW}(s,c)\mathbf{F}_W(c) + \mathbf{C}_{UU}(s,c)\mathbf{F}_U(c) + \mathbf{C}_{UV}(s,c)\mathbf{F}_V(c) = \mathbf{U}(s), \tag{23}$$

$$\mathbf{C}_{VW}(s,c)\mathbf{F}_W(c) + \mathbf{C}_{VU}(s,c)\mathbf{F}_U(c) + \mathbf{C}_{VV}(s,c)\mathbf{F}_V(c) = \mathbf{V}(s). \tag{24}$$

Before the system defined by equations (23) and (24) can be solved for $\mathbf{F}_U(s)$ and $\mathbf{F}_V(s)$[1], the unknown right-hand-side displacement fields $\mathbf{U}(s)$ and $\mathbf{V}(s)$ must be eliminated. This is subsequently done using the consequences of sticky contact.

In small deformations, using equation (1), the horizontal components of the differential speed vector in directions x and y, at contact points, are given by

$$w_{tx} = V_s\left(1 + \frac{\partial u}{\partial x}\right) - R(y)\Omega, \text{ where } R(y) = \sqrt{R^2 - y^2}, \tag{25}$$

$$w_{ty} = V_s\left(\frac{\partial v}{\partial x}\right). \tag{26}$$

At any stick-contact point, w_{tx} and w_{ty} are equal to zero. Since V_s and Ω are global constants, it follows that $\frac{\partial u}{\partial x}$ and v remain constant along any segment parallel to the x-axis, within the stick-contact area. All components in $\mathbf{U}(s)$ and $\mathbf{V}(s)$ may hence be related to $2 \times K_{st}$ constants, where K_{st} corresponds to the number of nodal rows containing stick-contact nodes. These constants are so far unknown and thus require $2 \times K_{st}$ additional equations which are obtained by enforcing continuity of $\frac{\partial u}{\partial x}$ and v, in direction x, across the leading edge stick-contact nodes.

Referring to figure 2, let $N_{i,j} = N(i, j) = (j-1)K_x + i$ be the global number of a stick-contact node at position $(x, y) = \left((2i - K_x - 1)\frac{a_x}{2}, (2j - K_y - 1)\frac{a_y}{2}\right)$. Also, let $i_{ref}(j)$ designate the x-direction index of the leading edge stick-contact node along the nodal row j. Using a finite difference approach and letting $R_j = R\left(\left(2j - K_y - 1\right)\frac{a_y}{2}\right)$, equations (25) and (26) lead to

$$\mathbf{U}\left(N_{i,j}\right) = \mathbf{U}\left(N_{i_{ref}(j)+1,j}\right) - \left(i_{ref}(j) + 1 - i\right) a_x \left(R_j \frac{\Omega}{V_s} - 1\right), \tag{27}$$

$$\mathbf{V}\left(N_{i,j}\right) = \mathbf{V}\left(N_{i_{ref}(j)+1,j}\right). \tag{28}$$

The $2 \times K_{st}$ quantities $\mathbf{U}\left(N_{i_{ref}(j)+1,j}\right)$ and $\mathbf{V}\left(N_{i_{ref}(j)+1,j}\right)$ in equations (27) and (28) correspond to the horizontal displacements of the nodes that are immediately adjacent to the leading edge contact node in each row. They can be related back to the main unknown fields $\mathbf{F}_U(s)$ and $\mathbf{F}_V(s)$ using system (5), which yields

$$\mathbf{U}\left(N_{i_{ref}(j)+1,j}\right) = \mathbf{C}_{UW}(N_{i_{ref}(j)+1,j}, c)\mathbf{F}_W(c) + \mathbf{C}_{UU}((N_{i_{ref}(j)+1,j}, c)\mathbf{F}_U(c) + \mathbf{C}_{UV}(N_{i_{ref}(j)+1,j}, c)\mathbf{F}_V(c), \tag{29}$$

$$\mathbf{V}\left(N_{i_{ref}(j)+1,j}\right) = \mathbf{C}_{VW}(N_{i_{ref}(j)+1,j}, c)\mathbf{F}_W(c) + \mathbf{C}_{VU}((N_{i_{ref}(j)+1,j}, c)\mathbf{F}_U(c) + \mathbf{C}_{VV}(N_{i_{ref}(j)+1,j}, c)\mathbf{F}_V(c). \tag{30}$$

The rotational speed Ω appearing in expression (27) is also unknown and thus requires one additional equation provided by the equilibrium of moments about the horizontal axis of the sphere parallel to Oy

$$\mathbf{q}_R^T(s)\mathbf{F}_U(s) = -T - \mathbf{x}^T(c)\mathbf{F}_W(c) - \mathbf{q}_R^T(\bar{s})\mathbf{F}_U(\bar{s}), \tag{31}$$

where $\mathbf{q}_R$ is a column vector defined for all contact nodes $M_{i,j} = M(i, j)$ as

$$\mathbf{q}_R(M_{i,j}) = R_j \sqrt{1 - \left(\frac{\mathbf{x}(M_{i,j})}{R_j}\right)^2}. \tag{32}$$

---

[1] $\mathbf{F}_U(s)$ and $\mathbf{F}_V(s)$ are unknown subvectors of $\mathbf{F}_U(c)$ and $\mathbf{F}_V(c)$, respectively.

On the other hand, systems (23) and (24) may be rewritten such that each line corresponds to a stick-contact node $N_{i,j}$ as follows

$$\mathbf{C}_{UW}(N_{i,j}, c)\mathbf{F}_W(c) + \mathbf{C}_{UW}(N_{i,j}, c)\mathbf{F}_U(c) + \mathbf{C}_{UV}(N_{i,j}, c)\mathbf{F}_V(c) = \mathbf{U}(N_{i,j}), \tag{33}$$

$$\mathbf{C}_{VW}(N_{i,j}, c)\mathbf{F}_W(c) + \mathbf{C}_{VU}(N_{i,j}, c)\mathbf{F}_U(c) + \mathbf{C}_{VV}(N_{i,j}, c)\mathbf{F}_V(c) = \mathbf{V}(N_{i,j}). \tag{34}$$

Combining equations (27)-(34), eliminating $\mathbf{U}(N_{i,j})$ and $\mathbf{V}(N_{i,j})$ and further rearranging the terms results in the final expression of a linear system in $\mathbf{F}_U(s)$, $\mathbf{F}_V(s)$ and Ω, to be solved at each iteration of the 3D stick-slip subroutine

$$\begin{aligned}
&\mathbf{G}_{UU}(N_{i,j}, s)\mathbf{F}_U(s) + \mathbf{G}_{UV}(N_{i,j}, s)\mathbf{F}_V(s) + \left(g_{ij}R_j/V_s\right)\Omega = \ldots \\
&\qquad\qquad g_{ij} - \mathbf{G}_{UW}(N_{i,j}, c)\mathbf{F}_W(c) - \mathbf{G}_{UU}(N_{i,j}, \bar{s})\mathbf{F}_U(\bar{s}) - \mathbf{G}_{UV}(N_{i,j}, \bar{s})\mathbf{F}_V(\bar{s}),
\end{aligned} \tag{35}$$

$$\begin{aligned}
&\mathbf{G}_{VU}(N_{i,j}, s)\mathbf{F}_U(s) + \mathbf{G}_{VV}(N_{i,j}, s)\mathbf{F}_V(s) + 0 \times \Omega = \ldots \\
&\qquad\qquad - \mathbf{G}_{VW}(N_{i,j}, c)\mathbf{F}_W(c) - \mathbf{G}_{VU}(N_{i,j}, \bar{s})\mathbf{F}_U(\bar{s}) - \mathbf{G}_{VV}(N_{i,j}, \bar{s})\mathbf{F}_V(\bar{s}),
\end{aligned} \tag{36}$$

$$\mathbf{q}_R^T(s)\mathbf{F}_U(s) + \mathbf{0}^T(s)\mathbf{F}_V(s) + 0 \times \Omega = -T - \mathbf{x}^T(c)\mathbf{F}_W(c) - \mathbf{q}_R^T(\bar{s})\mathbf{F}_U(\bar{s}), \tag{37}$$

where the following quantities are defined for convenience:

$$\begin{aligned}
&g_{ij} = (i_{ref}(j) + 1 - i)a_x\,, \qquad \text{and} \\
&\mathbf{G}_{AB}(N_{i,j}, :) = \mathbf{C}_{AB}(N_{i,j}, :) - \mathbf{C}_{AB}(N_{i_{ref}(j)+1,j}, :), \text{ for } A, B \in \{U, V, W\}\,.
\end{aligned}$$

A notable advantage of formulation (35)-(37) is that it avoids augmenting the system with $2 \times K_{st}$ additional unknown displacements $\mathbf{U}\left(N_{i_{ref}(j)+1,j}\right)$ and $\mathbf{V}\left(N_{i_{ref}(j)+1,j}\right)$, by analytically eliminating those quantities.

In order to avoid unnecessary coordinate transformations, Coulomb's law of friction is applied to F_W, F_U and F_V, instead of F_R, F_Φ and F_Θ, which is a valid approximation under small deformations. After solving system (35)-(37) for $\mathbf{F}_U(s)$, $\mathbf{F}_V(s)$ and Ω, the nodal horizontal displacement fields $\mathbf{U}$ and $\mathbf{V}$ are computed by means of system (5) and the differential speed components reevaluated at all slipping nodes using equations (25) and (26). It is then determined whether each currently sticking contact node N should be considered as a slipping node in the following iteration, by checking whether the latest computed friction and relative speed at N have exceeded the corresponding limits, i.e.

$$\left[\mathbf{F}_U^2(N) + \mathbf{F}_V^2(N) > \mu^2\mathbf{F}_W^2(N)\right] \text{ and } \left[w_{t_x}^2(N) + w_{t_y}^2(N) > w_{th}^2\right], \tag{38}$$

where w_{th} is a differential speed threshold, set to a small value. Reciprocally, each currently slipping node M is checked in order to determine whether it should be considered, in the sequel, as a stick-contact node. This is done by comparing the current differential speed at M to the threshold

$$w_{t_x}^2(N) + w_{t_y}^2(N) < w_{th}^2. \tag{39}$$

The sets "s" and "$\bar{s}$" of stick/slip nodes are updated accordingly and the limiting friction applied to slipping nodes in the current slipping direction given by w_{tx} and w_{ty}. This includes previously-determined (and still currently) slipping nodes for which the direction of maximum friction is updated such that it matches the latest direction of relative movement.

4.3. 3D combined algorithm

Following a similar approach to the one described in section 3.3 for the two dimensional case, the normal-contact subroutine and the stick-slip subroutine are combined starting with $\mathbf{F}_U = \mathbf{F}_V = 0$ and converging towards the actual solution of the three-dimensional and frictional rolling contact problem.

After convergence, the rolling resistance may be obtained from the following general expression

$$R_r = \sum \mathbf{F}_U + \frac{T\Omega}{V_s}. \tag{40}$$

The methodology described throughout section 4 was implemented and tested on the three-dimensional model of a rigid sphere, rolling in steady-state on an incompressible viscoelastic foundation of finite thickness. It showed to be robust and efficient: full convergence, based on the relative change in all the outputs, was typically obtained in 7 iterations.

5. Examples

In the following two examples, we consider the steady-state rolling with friction of a cylinder (in 2D) and a sphere (in 3D), both of radius $R = 2$ cm at a linear speed $V_s = 5$ cm/s on a viscoelastic layer of thickness $H = 5$ mm and density $\rho = 1000$ kg/m^3. At the contact interface, the coefficient of friction is assumed to be constant and equal to $\mu = 0.2$.

In both cases, the layer's material is modeled by a three-parameter viscoelastic solid whose master curves are given by

$$\begin{aligned} G'(\omega) &= G_0(1+f)\frac{(1+f)+\omega^2\tau^2}{(1+f)^2+\omega^2\tau^2}, \\ G''(\omega) &= G_0(1+f)\frac{f\omega\tau}{(1+f)^2+\omega^2\tau^2}, \end{aligned} \tag{41}$$

where $G_o = G'(0) = 3.0$ MPa is the static shear modulus, $\tau = 0.25$ s is the creep time and $f = G'(0)/G'(\infty) - 1 = 1$.

The layer's behavior is described by means of boundary element formulations of the form given by (2) where compliance matrices are formed using the methods proposed by Qiu (2006) and Zéhil and Gavin (2013b), in two and three dimensions respectively. Following these references' notations, the spatial periods are set equal to $L = L_x = L_y = 20$ cm which, at the given speed, allows for sufficient creep recovery of the foundation layer between two successive arrivals of moving objects and therefore enforces aperiodicity. Spacings between nodes are set equal to $a = a_x = a_y = 0.25$ mm. With these choices of L and a, retaining 2000 terms in the series yields stable matrices of sufficient accuracy (see Zéhil and Gavin, 2013b, table 1).

5.1. *Rigid cylinder on a viscoelastic foundation in 2D*

In this first example, a cylinder is rolling under the influence of a distributed horizontal load Q (per unit length) applied along its upper generatrix (i.e. accompanied by a driving torque $T = QR$). A concomitant distributed vertical load $P = 20$ kN/m is applied along the cylinder's axis. The corresponding mean vertical pressure is of 2.58 MPa, which is about the same as for the sphere in section 5.2. The two-dimensional rolling contact problem is solved following the guidelines presented in section 3 and some of the main results are reported below.

Surface displacements are plotted in figure 3 along with a horizontal line indicator showing the stick-contact area and the slipping regions, as determined by the 2D stick-slip subroutine. Given the current geometry, loading, speed, interface and foundation characteristics as well as the discretization, slipping occurs at the leading edge of the contact surface (1 node) and to a greater extent, at its trailing edge (counting 3 nodes). It may be noted that, due to viscoelasticity, the deformation fields are asymmetrical. Indeed, the contact surface extends further to the front (i.e. in the direction of movement) as the foundation material looses contact with the cylinder at a higher ordinate than it does at the trailing edge. As implemented in the last equation of system (16), the horizontal displacement $u(x, H)$ keeps a constant slope across the stick-contact region, which, according to (15), reflects the absence of relative movement between touching points. It is also noteworthy that $u(x, H)$ takes a steeper slope in the slipping region at the back of the cylinder, which indicates that in that region, given (1) and (15), the cylinder is slipping forwards relative to the foundation and hence is, consistently with what appears on figure 4, applying to it the maximum contact shear in the positive direction.

The contact stress fields are given in figure 4 along with the same contact nature indicator. The normal stress distribution is clearly asymmetrical, giving rise to a viscoelastic rolling resistance. In the slip-contact zone, at the back of the rolling cylinder, the tangential stress field follows the shape of the normal stress field, scaled by $-\mu$. It may also be noted that the negative area between the curve $\tau(x, H)$ and the horizontal axis at the front, is slightly larger than the positive one located at the back. Hence as expected, the shear stress distribution generates a moment about the cylinder's axis balancing the driving torque $T = QR$.

5.2. *Rigid sphere on a viscoelastic foundation in 3D*

A horizontal point load Q is now applied at the top of a sphere, pushing it forward in direction x. The sphere is assumed to be rolling in steady state, without spinning about its vertical axis z. As in section 5.1 a driving torque $T = QR$ about the center of the sphere is accounted for. A concomitant point load $P = 150$ N is applied vertically

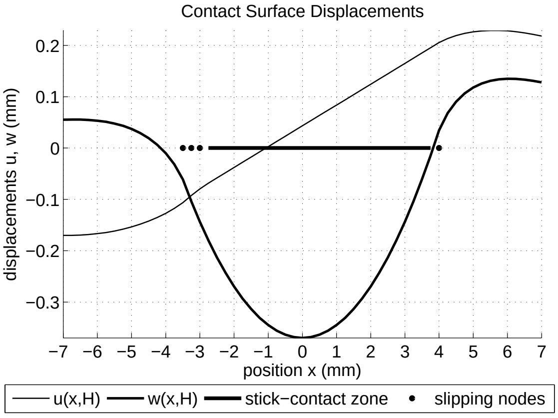

Figure 3: Foundation surface displacements

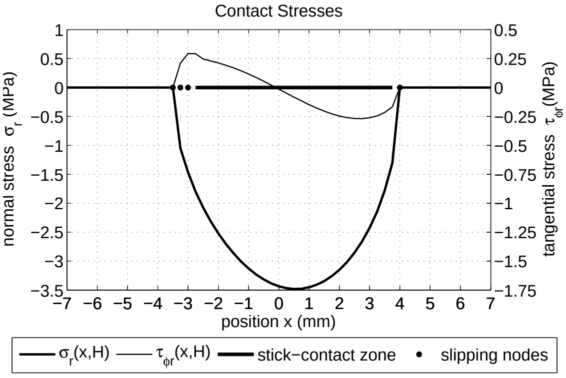

Figure 4: Surface contact stress fields

at the center. Load P was chosen such that the mean vertical pressure on the foundation (which is of 2.56 MPa) be approximately the same as for the cylinder in section 5.1.

The corresponding three-dimensional rolling contact problem is solved according to the principles exposed in section 4. Some of the main results are presented hereafter.

Figure 5 reveals two different regions, in terms of contact nature, across the contact interface. Slipping occurs over a crescent-shaped region at the back of the sphere while its remaining contact surface sticks to the subbase. Referring to its dimension in the direction of movement, the slip-contact zone appears to be thicker on the sides than it is in the central part of the contact interface. This observation may be explained by the greater vertical pressure acting in the middle (see figures 6), which increases the slipping threshold in that region.

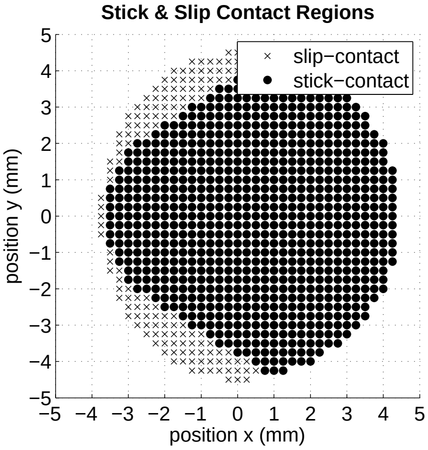

Figure 5: Stick and slip-contact regions

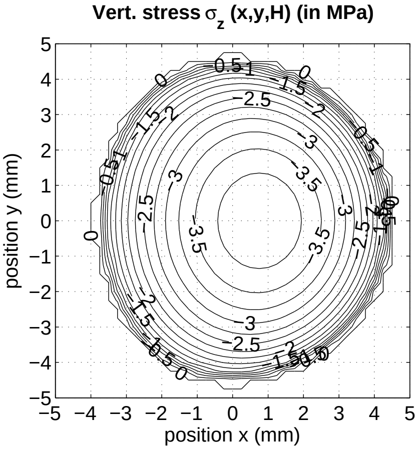

Figure 6: Contour plot of $\sigma_z(x, y, H)$

Figure 6 shows a contour plot of the vertical stress field over the contact area. Minor irregularities in the outline are due to the rectangular mesh following a curved path. The asymmetrical shape of $\sigma_z(x, y, z = H)$ is comparable to the one presented for $\sigma_z(x, H)$ in figure 4 in the case of a rolling cylinder. It mainly results from the time-dependent behavior of the foundation strip and opposes a viscoelastic resistance to the rolling of the sphere. Simplified approaches to estimating the 3D rolling resistance on a sphere, based on the observed similarities between 2D and 3D solutions, are presented by Zéhil and Gavin (2013a).

A contour plot of the horizontal stress field in the direction of movement (i.e. direction x), across the contact surface, is given in figure 7. The corresponding surface plot may be seen on figure 8. It has marked similarities with the tangent contact stress field $\tau_{xz}(x, H)$ presented in figure 4 for the 2D cylinder. Indeed, performing a vertical cut parallel to the x-axis on the central part of figure 8 would yield a very similar shape to the one obtained in the two-dimensional case.

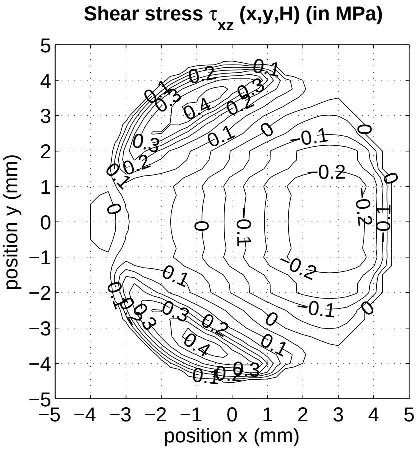

Figure 7: Contour plot of $\tau_{xz}(x, y, H)$

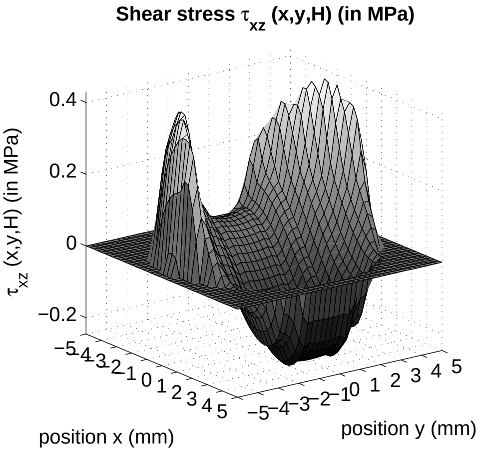

Figure 8: Surface plot of $\tau_{xz}(x, y, H)$

While it is rolling clockwise, the sphere rubs against the foundation pushing it backwards in the front part of the stick-contact zone, which explains the negative sign of τ_{xz} on the corresponding region of the plots. In contrast, the sphere slides forward on the lateral slip-contact areas at the back, hence shearing the subbase in the direction of movement and yielding a positive sign of τ_{xz}. These features are further described by the quiver plot given in figure 14. The latter also reveals that the divergence of the horizontal stress field is equal to zero in the vicinity of the point defined by $(x, y) = (-1, 0)$. Furthermore, the vertical and longitudinal contact stress distributions satisfy the moment equilibrium condition given by equation (37), which also involves the applied torque $T = QR$. As a consequence, the rolling resistance may be computed according to expression (40) yielding a value of 3.07 N, in the present case.

Figure 9 shows a contour plot of the transverse contact stress distribution. The field $\tau_{yz}(x, y, H)$ is antisymmetric with respect to the x-axis (i.e. odd in y). The corresponding resultant force is therefore equal to zero, which corresponds to an equilibrium condition that was not specifically enforced but is naturally satisfied by the algorithm. The sign of τ_{yz} reveals that, through surface interaction, the subbase is being transversally maintained as it moves away from the x-axis. This is consistent with information found on the quiver plot (figure 14) as well as on the plot of the lateral displacement field (figure 13). The maximum transverse projection of the horizontal stress, which is slightly above 0.4 MPa, is reached within the lateral slipping regions, near the interface with the stick-contact zone.

The vertical displacement field is shown in figures 10. It is asymmetrical, consistent with the vertical pressure field and may be compared to its two-dimensional counterpart given in figure 3. The contour lines of $w(x, y, z)$ are closer to each other at the front of the contact surface where the layer touches the cylinder about 0.1 mm higher than it does at its trailing edge. Indeed, from figure 5, the leading edge stick-contact nodes are positioned at $x = 4.25$ mm, while the trailing edge slip-contact nodes are located at $x = -3.75$ mm. The corresponding contour lines on figure 10 are $w = -0.12$ mm and $w = -0.22$ mm, respectively.

In this example, the foundation strip is made of an incompressible material. Consequently, the integral of $w(x, y, H)$ over a rectangular area of dimensions $L_x \times L_y$ centered at $(x, y) = (0, 0)$ should be equal to zero. This fact is however difficult to verify numerically since doing so would require discretizing the entire domain, which in this case, is much larger than the contact area. As a consolation, it may be noted that the level lines of w indicate a positive vertical displacement near the edges of the discretized surface.

A contour plot of the horizontal displacement field $u(x, y, H)$, in the direction of movement, is given in figure 11 across the entire candidate contact surface. Striking similarities of $u(x, y, H)$ may be noticed with its two dimensional counterpart $u(x, H)$ presented in figure 3 for the 2D cylinder. Indeed, it has a constant slope across each segment of constant ordinate (i.e. constant y) in the stick-contact zone, which may be seen directly on the surface plot in figure 12, or alternatively by noticing the constant spacing between contour lines in the same region of the contour plot.

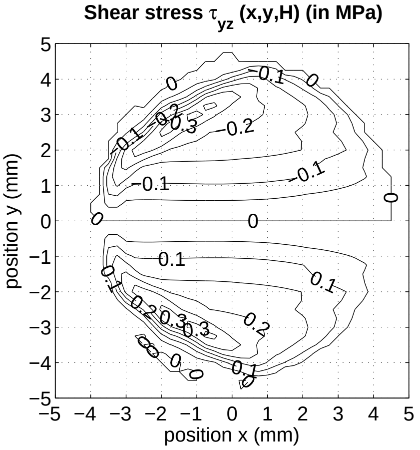

Figure 9: Contour plot of $\tau_{yz}(x, y, H)$

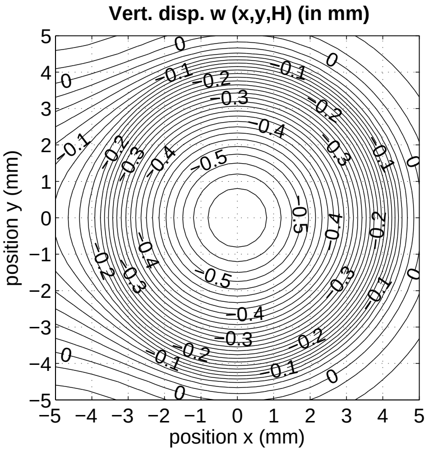

Figure 10: Contour plot of $w(x, y, H)$

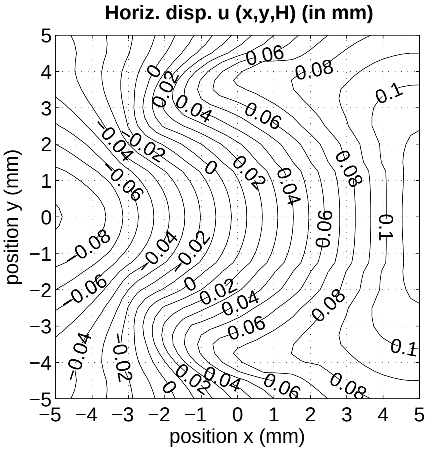

Figure 11: Contour plot of $u(x, y, H)$

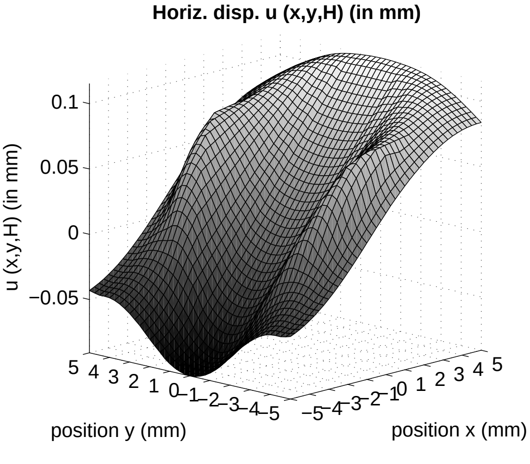

Figure 12: Surface plot of $u(x, y, H)$

Referring to equations (1) and (25), the constant slope of $u(x, y, H)$ in the stick-contact zone reflects the fact that w_{t_x} is equal to zero. Furthermore, the distance between consecutive level lines of $u(x, y, H)$, measured parallel to the x-axis, becomes clearly smaller in the lateral parts of the slipping region, which indicates that the sphere is slipping forwards relatively to the surface and hence applying to it a positive (limiting) shear stress. This is illustrated further by the quiver plot of the horizontal shear stress applied to the layer's surface, presented in figure 14, where it may also be seen that slipping occurs backwards in the thin central part of the slip-contact zone, which is consistent with an increased spacing between level lines on figure 11 in that same region.

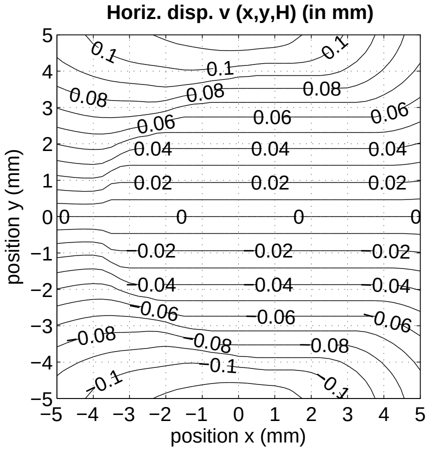

Figure 13: Contour plot of $v(x, y, H)$

Figure 13 shows the contour lines of the lateral displacement field. As expected, the level lines of $v(x, y, H)$ are parallel to the x-axis in the sticking region which, referring to (26), confirms that v is constant across segments of constant ordinate within the stick-contact zone where w_{t_y} is equal to zero.

The sign of v on figure 13 indicates that, as a result of vertical pressure, the sphere pushes the subbase laterally, away from its path as it is moving forward. Conversely, according to the quiver plot on figure 14, the sphere exerts surface frictions on the foundation that are oriented inwards (i.e. towards the central line of movement). As a result of these opposite actions, the lateral displacement field increases linearly with the distance from the centerline as revealed by the constant spacing, in the stick-contact zone, between level lines of v, on figure 13. In the slipping region, as well as in the vicinity of the contact area, surface interactions fade which causes the foundation to move further away as revealed by a closer spacing between contour lines of v. At a larger distance from the x-axis, the sphere's influence decreases and the lateral displacement field behaves accordingly.

A quiver plot of the absolute velocity field across the foundation's surface is given in figure 15. Consistently with all previous observations, it may be seen that, under the influence of the incoming sphere and as a result of continuum mechanics, the layer moves laterally away from the x-axis before it is actually reached by the sphere. Once it becomes part of the stick-contact area, the subbase is maintained by surface friction. It is swept under the sphere and travels backwards in a straight line. In the slip-contact regions, the frictional limit is exceeded and the layer's surface moves away from the x-axis under the influence of unbalanced volume forces. Behind the sphere, the foundation's surface starts recovering its original configuration. Comparing local inclinations of the velocity field, between regions that are located in front and at the back of the moving sphere, one can tell that recovery occurs at a slower rate than the one at which deformation takes place. Beyond the local disturbances of the velocity field, which may be associated with wake effects in fluids, and are due to friction, this observation is further explained by the time-dependent behavior of the foundation material. The rates at which displacements occur depend on the relaxation spectrum of the viscoelastic layer. In the present case whereby a simple three-parameter model is used, with f set equal to 1, the creep time is twice as large as the relaxation time.

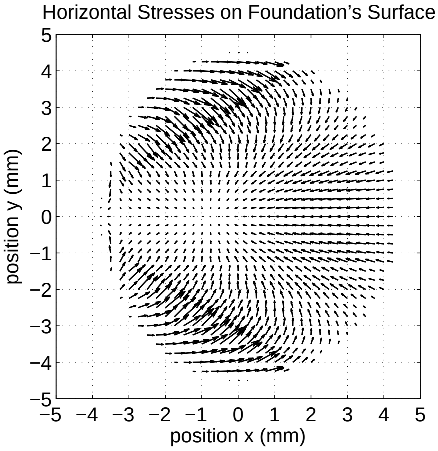

Figure 14: Horizontal stresses on foundation's surface (quiver plot)

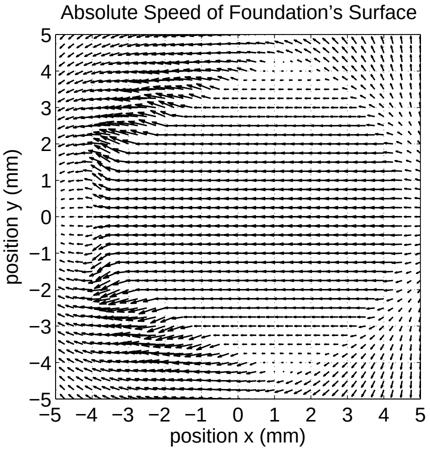

Figure 15: Absolute speed of foundation's surface (quiver plot)

6. Conclusion

Simple algorithms for solving steady-state frictional rolling contact problems in two and three dimensions were presented in this work. These algorithms constitute appealing alternatives to fully comprehensive contact solving strategies involving more complex implementations. In contrast with other 'simplified' theories based on very limiting assumptions, the cores of our contact algorithms only rely on general principles: (i) the "normal-contact" subroutine determines the (possibly discontinuous) contact surface by resolving geometrical conflicts and eliminating unacceptable surface tractions as they arise, and (ii) the "stick-slip" subroutine determines the (possibly discontinuous) regions of same tangential contact-nature by eliminating differential motions in the sticking regions and enforcing frictional limitations in the slipping regions. The proposed algorithms are formulated in the context of small deformations and applied to the cases of a rigid cylinder and a rigid sphere rolling on a linear viscoelastic layer of finite thickness, in two and three dimensions, respectively. These formulations pose no limitations regarding the layer's thickness or the viscoelastic model and are easily adapted to handle deformable indenters by solving for stresses and strains on two candidate contact surfaces simultaneously. The proposed contact algorithms can also be extended to problems including material nonlinearities, provided that the linear systems (12) and (16) in 2D, or (21) and (35)-(37) in 3D, are replaced by their nonlinear counterparts and handled using a suitable iterative solving scheme, embedded in the contact subroutines. Furthermore, the small-strain assumption can be dropped and the method extended to handle finite deformations by accounting for the horizontal displacements of the nodes while checking for geometrical conflicts. In order to illustrate the functioning of the proposed algorithms and demonstrate their capabilities, two application examples were treated. Results from the examples were presented, discussed and related to a certain extent. The algorithms showed to be robust and efficient at solving the two and three-dimensional rolling contact problems on which they were tried. It is noteworthy that full solutions to three-dimensional problems are undeniably rich and constitute an important contribution to understanding their underlying physics.

Acknowledgments

This material is based upon work supported by the National Science Foundation under Grant No. NSF-CMMI-0900324. Any opinions, findings, and conclusions or recommendations expressed in this material are those of the authors and do not necessarily reflect the views of the National Science Foundation.

References

Galin, L., Gladwell, G., 2008. Contact Problems: The Legacy of L.A. Galin. Solid Mechanics and Its Applications. Springer.

Hertz, H., 1881. Über die berührung fester elastischer körper (on contact between elastic bodies). Journal für die reine und angewandte Mathematik 92, 156–171.

Jaffar, M., 1997. A general solution to the axisymmetric frictional contact problem of a thin bonded elastic layer. Proceedings of the Institution of Mechanical Engineering 211 (7), 549–558.

Jaffar, M., 2008. On the frictionless axi-symmetric contact of a thick elastic layer and the associated squeeze film problem. Proceedings of the Institution of Mechanical Engineering Part J, Journal of Engineering Tribology 222 (1), 61–68.

Kalker, J. J., 1979. The computation of three-dimensional rolling contact with dry friction. International Journal for Numerical Methods in Engineering 14 (9), 1293–1307.

Love, A. E. H., 1927. A Treatise on the Mathematical Theory of Elasticity, 4th Edition. Cambridge University Press.

Munisamy, R., Hills, D., Nowell, D., 1991. Brief note on the tractive rolling of dissimilar elastic cylinders. International Journal of Mechanical Sciences 33 (3), 225–228.

Qiu, X., 2006. Full two-dimensional model for rolling resistance: hard cylinder on viscoelastic foundation of finite thickness. Journal of Engineering Mechanics 132 (11), 1241–1251.

Vollebregt, E. A. H., June 2012. The Finite Element Method for Solid and Structural Mechanics. VORtech Computing, Delft, The Netherlands.

Zéhil, G.-P., Gavin, H. P., 2013a. Simplified approaches to viscoelastic rolling resistance. International Journal of Solids and Structures 50 (6), 853 – 862.
URL `http://www.sciencedirect.com/science/article/pii/S002076831200409X`

Zéhil, G.-P., Gavin, H. P., 2013b. Three-dimensional boundary element formulation of an incompressible viscoelastic layer of finite thickness applied to the rolling resistance of a rigid sphere. International Journal of Solids and Structures 50 (6), 833 – 842.
URL `http://www.sciencedirect.com/science/article/pii/S002076831200491X`

Zienkiewicz, O. C., Taylor, R. L., Sep. 2005. The Finite Element Method for Solid and Structural Mechanics, 6th Edition. Butterworth-Heinemann.